Experimental investigation and modeling of the mechanical behaviour of Yanji swelling mudstone subjected to wetting-drying-freezing-thawing cycles

Zhixiong Zeng, Ling-Wei Kong, Yu-Jun Cui

Experimental investigation and modeling of the mechanical behaviour of Yanji swelling mudstone subjected to wetting-drying-freezing-thawing cycles

Zhixiong Zeng[1*], Ling-Wei Kong[2], Yu-Jun Cui[3]

[1]: Department of Civil and Environmental Engineering, Hong Kong University of Science and Technology, Hong Kong SAR, China

[2]: State Key Laboratory of Geomechanics and Geotechnical Engineering, Institute of Rock and Soil Mechanics, Chinese Academy of Sciences, Wuhan 430071, China

[3]: Laboratoire Navier/CERMES, Ecole des Ponts ParisTech, Champs-sur-Marne, 77455 Marne-la-Vallée cedex 2, France

***Corresponding author**

Research Assistant Professor Zhixiong Zeng, PhD

Department of Civil and Environmental Engineering
The Hong Kong University of Science and Technology
Clear Water Bay, Hong Kong
China
Tel.: +852 95025487
E-mail address: zhixiongzeng@ust.hk

Abstract: Rocks and soils in seasonally frozen regions are subjected to cyclic wetting-drying-freezing-thawing (WDFT) process. The influence mechanism of WDFT process on their mechanical behaviour is not fully understood and the existing constitutive models are not capable of capturing the strain-softening behaviour under WDFT cycles. In the present study, a series of consolidated drained triaxial compression and mercury intrusion porosimetry tests were performed on Yanji mudstone subjected to WDFT cycles. Results indicated that the WDFT cycles could induce a large amount of cracks and large pores between aggregates and compress the aggregates with a decrease of the intra-aggregate pores. After cyclic WDFT process, the specimens exhibited more significant strain-softening and dilative behaviour. The elastic modulus, peak and residual shear strengths of the mudstone decreased significantly with increasing WDFT cycles, especially in the case of low confining pressures. These decreases were more pronounced in the first four cycles and became negligible after 4 cycles. As the cyclic number increased, the cohesion of specimens decreased remarkably owing to the presence of cracks and the destruction of bonds between aggregates. By contrast, the effective friction angle, Poisson's ratio and dilatancy angle increased with the WDFT cycles due to the more compact aggregates induced by the high suction during drying process. A nonlinear elastic constitutive model was developed for describing the strain-softening behaviour of Yanji mudstone subjected to WDFT cycles. The deviator stress-axial strain relationship predicted by the proposed model agreed well with the measured one, indicating the relevance of the predictive model.

Keywords: swelling mudstone; wetting-drying-freezing-thawing cycle; stress-strain behaviour; microstructure; modelling

1 Introduction

Swelling rock and soils correspond to the deposits composed of large amounts of clay minerals (e.g. montmorillonite and illite). These deposits are widely found in more than 60 countries such as Australia, China, Sudan, Spain, USA, etc [1, 2]. Due to the special mineralogical compositions, swelling rocks and soils are diverse in appearance and hydro-mechanical properties. They can develop significant swell or swelling pressure after contact with water, and shrink upon desiccation. Additionally, they might exhibit an acceptable strength in dry condition while soften significantly upon the presence of water [1, 3]. These variable properties cause severe distress to the associated geotechnical infrastructures, such as non-uniform settlement, pavement cracking, and slope failure [4-7]. It is therefore essential to thoroughly evaluate the mechanical behaviour of swelling rocks and soils to achieve a reliable design and operation of geotechnical infrastructures.

Over the past decades, many studies attempted to address the couplings between changes in water content and the induced modifications in fabric and mechanical property for swelling rocks and soils [8-12]. It was documented that the swelling behaviour of swelling rocks and soils could be influenced by many factors, including moisture content, dry density and clay mineral content [13-15]. Generally, the final swelling pressure and swelling strain increased as the initial dry density and clay mineral content increased. By contrast, as the initial water content increased, the final swelling pressure or swelling strain decreased [16-18]. After swelling, the breakage of cementation between particles would lead to a significant reduction of shear strength. Furthermore, a lower initial water content could more significantly reduce the shear strength due to the larger swelling deformation upon wetting [19-21].

Additionally, the mechanical properties of swelling rocks and soils can be possibly altered by cyclic climate loadings [22-26]. In this regard, most common environmental factor is wetting-drying (WD) cycles. Nowamooz and Masrouri [27, 28] indicated that the successive WD processes induced a progressive accumulation of irreversible strains, and the loose and dense expansive soil specimens achieved a unique final state after several cycles. Additionally, the desiccation and shrinkage could facilitate the crack propagation, and the crack surface became more irregular and coarse with repeated WD [29]. Such irreversible strain and cracks led to the destruction of bonds and resulted in degradation of the hydro-mechanical behaviour of the swelling rocks and soils [23, 28, 30].

Recently, there is a rapid increase of geotechnical constructions in seasonally frozen regions due to significant residential land and transportation network developments [31, 32]. In these regions, the rocks and soils are subjected to not only seasonal WD cycles, but also frequent freezing-thawing (FT) process [7, 33]. During freezing, the formation of ice lenses would modify their structure on the micro and macro-scales and reduce their integrity [34, 35]. After FT cycles, the large-pore volume increased and the surface crack propagated [32, 36]. These large pores and cracks not only led to a larger hydraulic conductivity [37, 38] but also weakened the rocks and soils in terms of loss in strength and stiffness [7, 39, 40].

In many seasonally frozen regions with monsoon climates, winters are cold with frequent and heavy snowfall, and summers are hot with sufficient rainfall. It would be more relevant to take into account the influences of both WD and FT processes. However, most of previous researches focused on the mechanical behaviour of swelling rocks and soils subjected to separate WD or FT

process. In spite of some recent works by Zhao et al. [6] and Zhu et al. [41], the information about the mechanical properties under the combined action of WD and FT cycles is quite scarce and the influence mechanism of wetting-drying-freezing-thawing (WDFT) cycles has not been fully understood. In addition, the swelling rocks and soils can possess a significant strain-softening behaviour due to their relatively high fragility especially after cyclic WD process, and it becomes essential to capture the strain-softening behaviour in the simulation of slope progressive failure under WDFT cycles. However, the existing constitutive models are not capable of characterising the strain-softening behaviour for swelling rocks and soils subjected to WDFT cycles.

In the present work, a series of consolidated drained (CD) triaxial compression tests under different confining pressures were carried out on Yanji swelling mudstone specimens subjected to various WDFT cycles, and the effect of WDFT on the Young's modulus, peak and residual shear strengths, effective friction angle, effective cohesion, Poisson's ratio and dilatancy angle was determined. In parallel, the microstructure evolution of swelling mudstone during WDFT cycles was also investigated using MIP technique, enabling the deterioration mechanism of those mechanical properties to be advanced. Additionally, a nonlinear elastic constitutive model considering the WDFT effect was proposed to further simulate the triaxial stress-strain behaviour of mudstone specimens. The predictive performance of the proposed model was verified using the test results.

2 Materials and Experimental methods

2.1 Materials

104 The study area is located at the Yanji section of Jilin-Hunchun railway line, where a great number of
105 mudstone cut slopes failed after rainfalls (Fig. 1a). Subsequently, many excavation works and
106 reinforcement measures, such as anti-slide piles, arch grille beams and retaining walls, were
107 conducted after the failure of cutting slopes [19]. The mudstone samples were extracted from a
108 typical K275 landslide (Fig. 1b). Table 1 summarises the geotechnical properties and mineralogical
109 composition of the mudstone. The specific gravity, liquid limit, plastic limit and shrinkage limit of
110 the mudstone are 2.72, 41.4%, 15.8%, and 13.9%, respectively. The mudstone has a natural dry
111 density of 1.67 Mg/m^3, a natural water content of 20.0% and a liquidity index of 0.16. Its free
112 swelling ratio and volume shrinkage ratio are 54% and 14%, respectively, defining a low swell
113 potential [42]. For the measurement of shrinkage characteristics, a specimen with natural water
114 content and dry density was prepared and then dried until the specimen mass decreased to a constant
115 value. The shrinkage limit was determined at the inflection point where the increasing rate of
116 shrinkage strain changed significantly with the decreasing water content. From the X-ray diffraction
117 (XRD) analysis (Fig. 2), the dominant clay mineral of the mudstone is montmorillonite (23.0%), with
118 others being illite, feldspar, quartz and dolomite. The maximum dry density and the optimum water
119 content of the mudstone were also determined by standard Proctor compaction test, equal to 1.72
120 Mg/m^3 and 20.6%, respectively.

121 As shown in Fig. 1a, the mudstone was subjected to extensive crushing and backfilling works
122 during the landslide remediation and the original structure of the mudstone was greatly disturbed by
123 the artificial activities [43]. To represent field conditions, the tested mudstone was first air dried and
124 then crushed to less than 2 mm. The grain size distribution of the crushed mudstone is shown in Fig. 3.

125 The grains larger than 0.075 mm and those smaller than 0.075 μm were measured by the wet-sieving
126 and hydrometer methods, respectively. The mean grain diameter (D_{50}) of crushed mudstone is 0.068
127 mm and the clay-size fraction is 7.4%.

128

129 **Fig. 1** Sample site and extracted sample: (a) the mudstone slope at the K275 section of Jilin-Hunchun
130 railway line, and (b) the swelling mudstone in a 4.0 m deep trench
131
132 **Table 1** Characteristics of the studied mudstone

Property		Value
Water content (%)		20.0
Dry density (Mg/m^3)		1.67
Specific gravity		2.72
Void ratio		0.63
Liquid limit (%)		41.4
Plasticity index		15.8
Free swelling ratio (%)		54
Volume shrinkage ratio (%)		14.0
Contraction coefficient		0.49
Shrinkage limit (%)		13.9
Maximum dry density (Mg/m^3)		1.72
Optimum water content (%)		20.6
Mineral composition (%)	Montmorillonite	23.0
	Illite	5.2
	Dolomite	3.1
	Feldspar	45.2
	Quartz	23.5

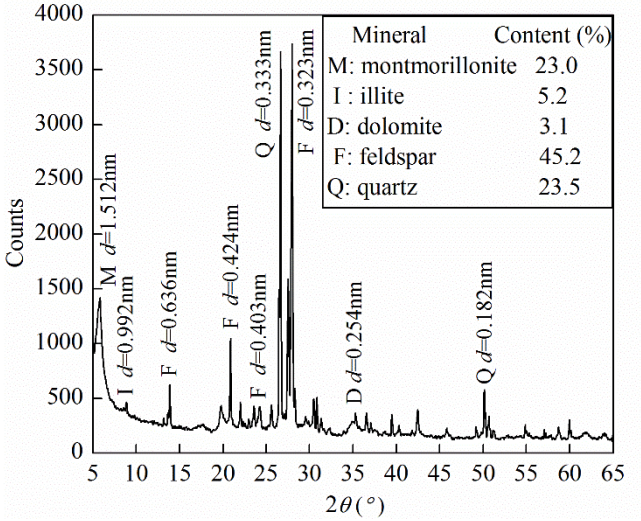

Fig. 2 X-ray diffraction pattern of the tested mudstone

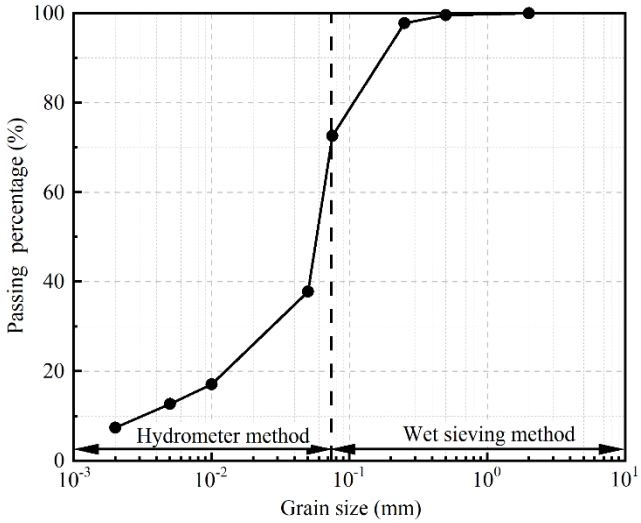

Fig. 3 Grain size distribution of the tested mudstone

2.2 Specimen preparation

In the field, the mudstone was crushed and compacted without adding more water in September 2013 because the natural water content was close to its optimum water content (20.6%). To simulate field conditions, the crushed mudstone was wetted by spraying deionised water to achieve a natural water content of 20.0%. The wet mudstone was mellowed in plastic bags for 48 hours for water homogenization. After that, the wet mudstone was subjected to static compaction to reach a dry density of 1.67 Mg/m^3, which corresponded to a compaction degree of 97%. The diameter and

height of obtained specimens are 61.8 and 125 mm, respectively. In this work, 64 specimens were prepared in total, with 4 specimens for each cycle.

In the study area, the monthly and daily mean temperatures are in the ranges of -13.2-21.7 ℃ and -18.2-29.3 ℃ while the relative humidity is 53-79%. To investigate the influence of climate condition on the mechanical behaviour, some of the prepared specimens were subjected to cyclic WDFT treatment using a temperature and humidity control box (Fig. 4). The detailed operating procedures of WDFT cycles are shown in Fig. 5. The specimens were first dried at a prescribed temperature (25 ℃) and a prescribed relative humidity (75%) in a temperature and humidity control box until the shrinkage limit of 13.9% was reached (Fig. 4b). Then, the they were vacuum saturated with deionised water and then subjected to drying at a prescribed temperature (25 ℃) and a prescribed relative humidity (75%) in the control box until the water content achieved the initial one (20.0%). Afterwards, freezing-thawing cycles were applied to the specimens. They were wrapped with plastic film and transferred to the control box of −15 ℃ for 12 h freezing (Fig. 4c). Subsequently, the specimens were stored at 15 ℃ for 12 h thawing. To account for the number of WDFT cycles (n), the specimens were subjected to 1, 2, 4, 6, and 8 cycles, respectively.

2.3 Experimental methods

The mechanical behaviour of specimens after various WDFT cycles was studied by CD triaxial tests using a conventional strain-controlled triaxial compression apparatus. The specimens were first vacuum saturated for more than 24 h. Then, a back pressure of 100 kPa and a cell pressure of 110 kPa were applied on the specimens to dissolve air bubbles for another 24 h. After that, the Skempton's B value was determined, larger than 0.98 for all tests. The cell pressure was increased

to the designed values of 150, 200, 300, and 400 kPa (corresponding to effective confining pressures of 50, 100, 200 and 300 kPa) for subsequent consolidation. Note that the adopted maximum confining pressure was determined according to the mudstone burial depth [19]. After that, according to ASTM D7181-20 [44], a shear rate as low as 0.015 mm/min was adopted for all tests, allowing a full dissipation of pore water pressure. During subsequent shearing, axial force and volume change were recorded. The tests ended when the axial strain reached 20%.

Fig. 4 WDFT process in the temperature and humidity control box: (a) test apparatus, (b) drying process, and (c) freezing-thawing (FT) process

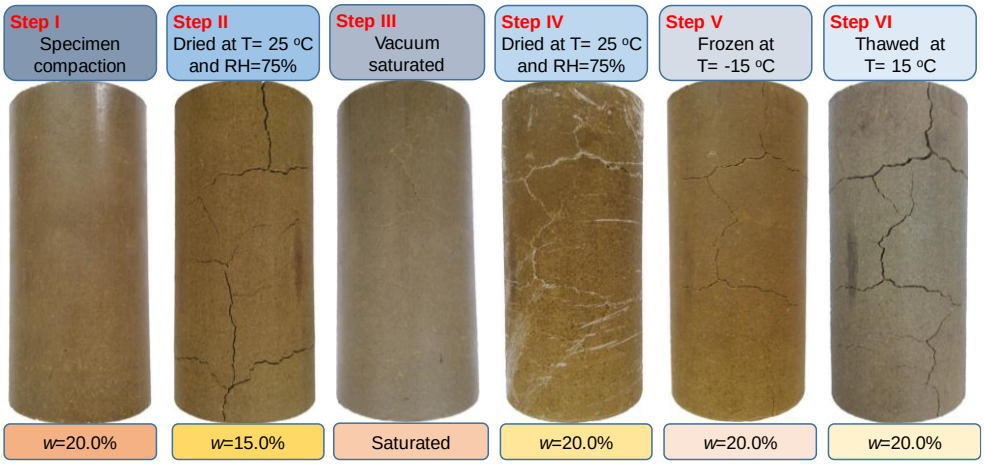

Fig. 5 Operating procedures of cyclic WDFT for Yanji swelling mudstone

To clarity the microstructure evolution of swelling mudstone with WDFT cycles, the pore size distributions of the as-compacted specimen (n=0) and those after various WDFT cycles (n=1, 2, 4, 6 and 8) were determined using an Autopore IV 9500 mercury intrusion porosimeter produced by Mike Co. The specimens were first cut into small cubes and rapidly frozen. After that, they were dried through sublimation in a vacuumed chamber for more than 24 h. During MIP test, the freeze-dried cube was placed into a low pressure chamber, and then a high pressure chamber. The working pressure increased from 3.6 to 200 MPa, allowing the pores with a diameter of 350 μm-6 nm to be detected.

3 Experimental results

3.1 Stress-strain behaviour

The variations of deviator stress (q) with axial strain (ε_1) for the as-compacted specimens (n=0) and those subjected to various WDFT cycles (n=1, 2, 4, 6 and 8) under different confining pressures (σ_3) are displayed in Fig. 6. For the specimens before WDFT cycles, the deviator stress increased rapidly at the beginning with the increase of axial strain, and then tended to stabilization, showing strain-hardening or slightly strain-softening behaviour. By contrast, for the specimens after WDFT cycles, the deviator stress increased, reached a peak and finally decreased, exhibiting remarkable strain-softening behaviour. Obviously, the deviator stress-axial strain curves of specimens subjected more WDFT cycles lied below those for less WDFT cycles. In addition, the lower the confining pressure, the more pronounced the influence of WDFT cycles on the stress-strain behaviour of specimens.

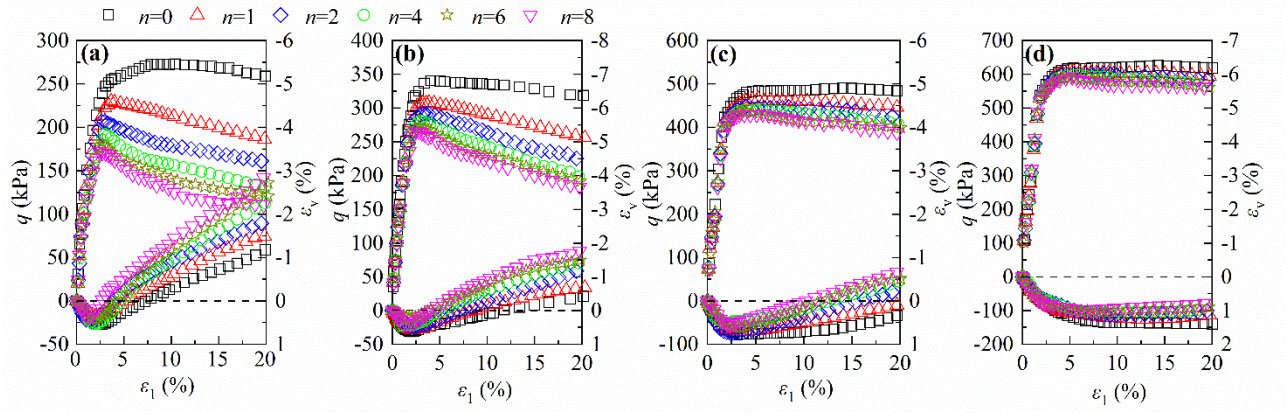

Fig. 6 Deviator stress and volumetric strain versus axial strain curves for the specimens before and after various WDFT cycles: (a) σ_3=50 kPa, (b) σ_3=100 kPa, (c) σ_3=200 kPa, and (d) σ_3=300 kPa

3.2 Volumetric strain

Fig. 6 also depicts the variations of volumetric strain (ε_v) with axial strain (ε_1) under various confining pressures before and after different WDFT cycles. For the specimens under low confining pressures, the volume change behaviour was characterized by contraction and subsequent dilatancy. Furthermore, the higher the cyclic number, the more significant the dilatancy behaviour. Nevertheless, the dilatancy was reduced with increasing confining pressure. As the confining pressure increased from 50 to 300 kPa, the contraction increased and the dilatancy decreased. In the case of a confining pressure of 300 kPa, pure contraction behaviour was identified especially for the specimens without application of WDFT cycles.

3.3 Elastic modulus and Shear strength

As schematically illustrated in Fig. 7, the elastic modulus, peak shear strength and residual shear strength can be determined from the deviator stress-axial strain curve. The elastic modulus represents the tangent modulus at the beginning of shearing and it is defined as the ratio of deviator stress to the axial strain in the range of 0%–1% [45]. The peak shear strength refers to the maximum deviator stress, while the residual shear strength is the asymptote of the deviator stress. Considering the

evolution law of deviator stress, the asymptote was determined by fitting the softening phase of deviator stress-axial strain curve using a logarithm function. As an example, the fitting results of the specimen 8 WDFT cycles and under a confining pressure of 50 kPa is presented in the Fig. 7. The deviator stress asymptotic value corresponds to the constant term of logarithm function (98.736 kPa). The variations of calculated elastic modulus, and peak and residual shear strengths against the number of WDFT cycles for the specimens under various confining pressures are summarized in Figs. 8 and 9. As expected, larger elastic modulus and peak shear strengths were identified for the specimens under a larger confining pressure, regardless of the WDFT cycles. From Fig. 8, it appeared that the elastic modulus declined with the increasing WDFT cycles for the specimens under a given confining pressure. Additionally, the decreasing rate reduced with the increase of WDFT cycles and it approached zero after the four cycles. A comparison of the specimens under various confining pressures showed that the decrease of shear strength was more pronounced for the specimens under a confining pressure of 50 kPa. For the specimens under a given confining pressure, both the peak and residual shear strengths decreased significantly at the four cycles and then tended to stabilise (Fig. 9), which was consistent with the observed WDFT effect on the elastic modulus. On the whole, the lower the confining pressure, the more significant the decreases of peak and residual shear strengths. The variation of the initial elastic modulus with peak shear strength for all the specimens is presented in Fig. 10. The elastic modulus increased with the peak shear strength. The relationship between the elastic modulus and peak shear strength can be well described using the following equation with a squared correlation coefficient R^2 as high as 0.969:

$$E_0=5547.603+79.081q_p \quad (1)$$

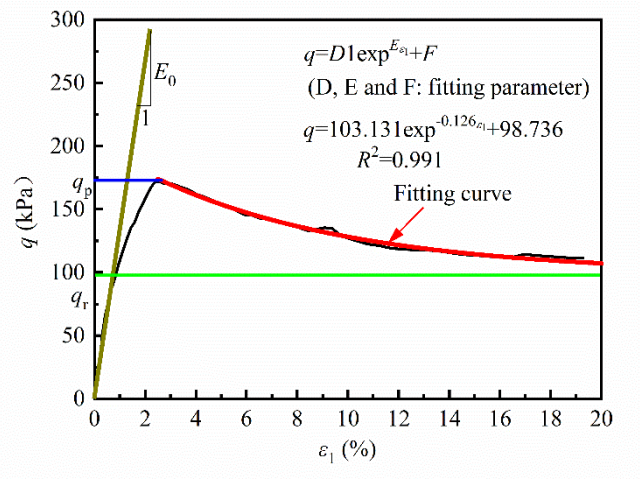

Fig. 7 Determination of elastic modulus E_0, peak shear strength q_p and residual shear strength q_r

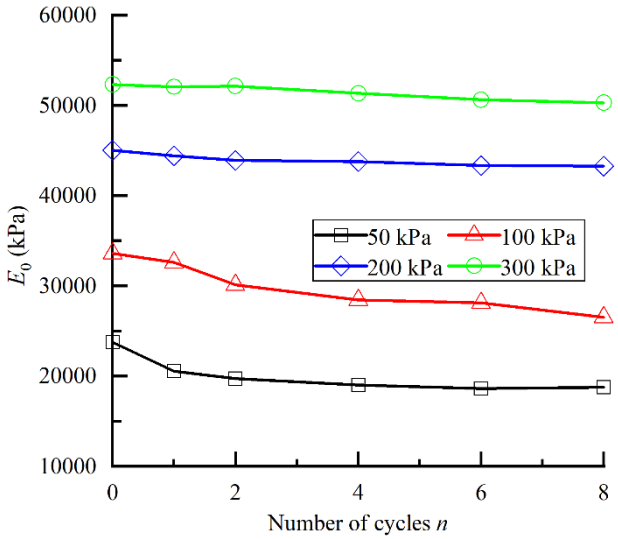

Fig. 8 Variations of elastic modulus with the number of WDFT cycles

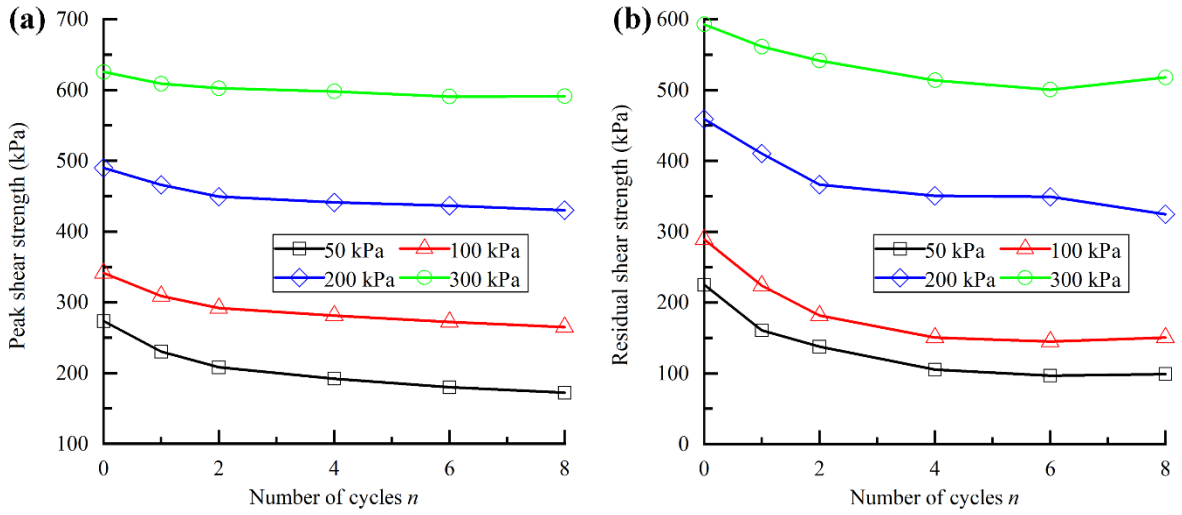

Fig. 9 Variations of peak and residual shear strengths with the number of WDFT cycles: (a) peak shear strength, and (b) residual shear strength

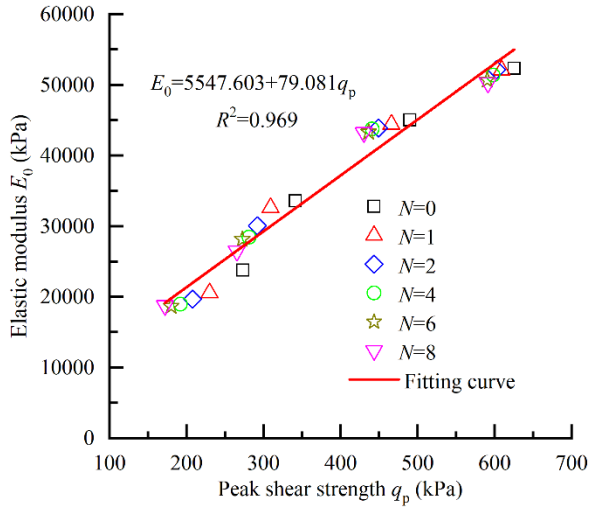

244

245 **Fig. 10** Relationship between of elastic modulus and peak shear strength

246

247 To further analyse the influence of WDFT cycles on the mechanical behaviour, the peak and

248 residual shear strengths are replotted in the plane of deviator stress (q) and mean effective stress (p')

249 in Fig. 11. As the cyclic number increased, the state lines at peak and critical states shifted down.

250 According to the state lines, the effective friction angle and effective cohesion at critical and peak

251 states can be determined using the following equations:

252 $$\sin\phi_{\mathrm{p}}^{'}=\frac{3M_p}{6+M_p} \tag{2}$$

253 $$c_{\mathrm{p}}^{'}=\frac{S_{\mathrm{p}}(3-\sin\varphi_{\mathrm{p}})}{6\cos\varphi_{\mathrm{p}}} \tag{3}$$

254 $$\sin\phi_{\mathrm{r}}^{'}=\frac{3M_r}{6+M_r} \tag{4}$$

255 $$c_{\mathrm{r}}^{'}=\frac{S_{\mathrm{r}}(3-\sin\varphi_{\mathrm{r}})}{6\cos\varphi_{\mathrm{r}}} \tag{5}$$

256 where M_p and M_r are the slopes of the peak and critical state lines, respectively, S_p and S_r are the

257 intercepts of the peak and critical state lines, $\phi_{\mathrm{p}}^{'}$ and $\phi_{\mathrm{r}}^{'}$ are the effective friction angles at the peak

258 and critical states, and $c_{\mathrm{p}}^{'}$ and $c_{\mathrm{r}}^{'}$ refer to the effective cohesions at the peak and critical states. Fig.

259 12 displays the variations of the effective friction angles and effective cohesions at peak and critical

states with the number of WDFT cycles. It could be observed that for all the specimens, the effective cohesion at peak state was significantly larger than the effective cohesion at critical state while the effective friction angle at peak state was slightly lower than that at critical state. As the cyclic number increased, the effective cohesions at both peak and critical states decreased significantly while the effective friction angles slightly. The relationships between the effective cohesion, effective friction angle and the number of WDFT cycles could be described using Eqs. (6-9):

$$c'_p=29.785+34.684e^{-0.535n} \quad (6)$$

$$c'_r=46.733e^{-0.754n} \quad (7)$$

$$\phi'_p=26.959-2.398e^{-0.512n} \quad (8)$$

$$\phi'_r=27.334-1.936e^{-1.226n} \quad (9)$$

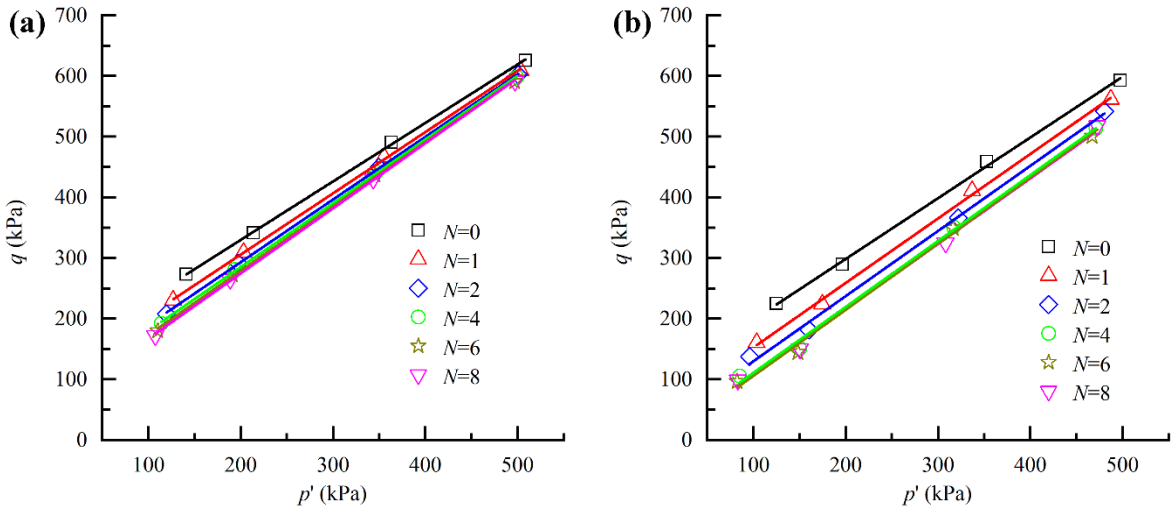

Fig. 11 State lines in the plane of deviator stress and mean effective stress: (a) peak state, and (b) critical state

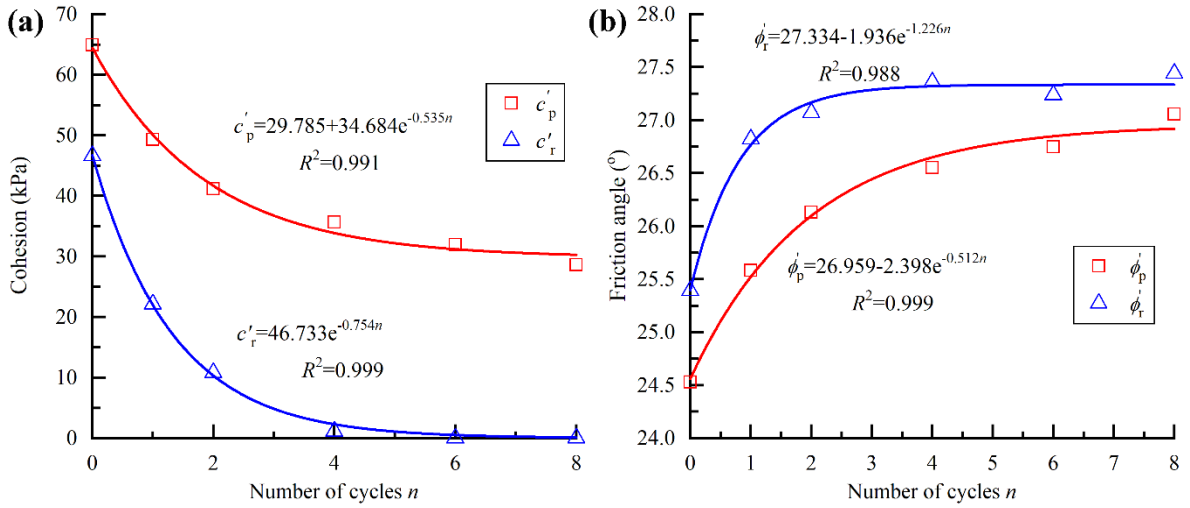

Fig. 12 Relationship between of peak and residual shear strength parameters, and the number of WDFT cycles: (a) effective cohesion, and (b) effective friction angle

3.4 Poisson's ratio and dilatancy angle

To further analyse the volume changes during shearing, the Poisson's ratio (ν) and dilatancy angle (ψ) were determined according to the volumetric strain-axial strain curves. As an example, Fig. 13 illustrates the deamination of Poisson's ratio and dilatancy angle. The slopes of volumetric strain-axial strain curves in the contractive and dilatancy phases are designated as k_c and k_D, respectively. These two parameters Poisson's ratio and dilatancy angle can be derived using Eqs. (10) and (11), respectively [46]:

$$\upsilon=\frac{1-k_c}{2} \tag{10}$$

$$\sin\psi=\frac{k_D}{-2+k_D} \tag{11}$$

Fig. 14a displays the variation of Poisson's ratio with WDFT cycles under various confining pressures. For the specimens under various confining pressures, the Poisson's ratio increased with the increasing cyclic number, albeit at a small increasing rate. After given WDFT cycles, the Poisson's ratio value decreased as the confining pressure increased, which was consistent with the volumetric

strain-axial strain relationships (Fig. 6). As the confining pressure increased, the specimens presented more contractive behaviour after given WDFT cycles. Fig. 14b presents the variations of dilatancy angle with the number of WDFT cycles under four various confining pressures. Note that the specimens with pure contractive behaviour are not included. For the specimens under given confining pressures lower than 200 kPa, the dilatancy angle increased with the increase of WDFT cycles, suggesting that the specimens after more WDFT cycles exhibited more pronounced dilative behaviour. For the specimens under a confining pressure of 300 kPa, the dialatancy angle were not noticeably influenced by the WDFT cycles. Additionally, the dialatancy angles of the specimens under a lower confining pressure was obviously larger than those of the specimens under a higher confining pressure, indicating the inhibition effect of confining pressure on the dilatant behaviour.

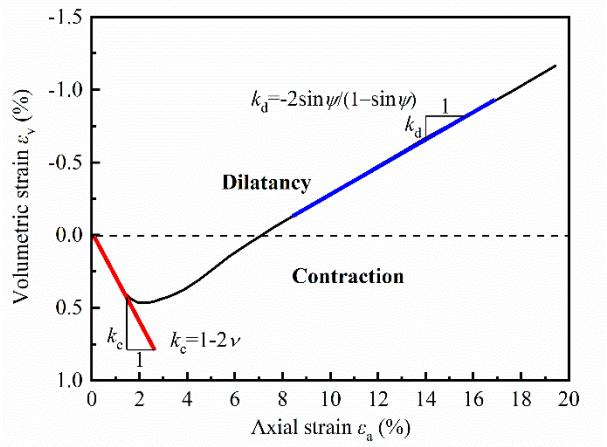

Fig. 13 Determined Poisson's ratio and dilatancy angle

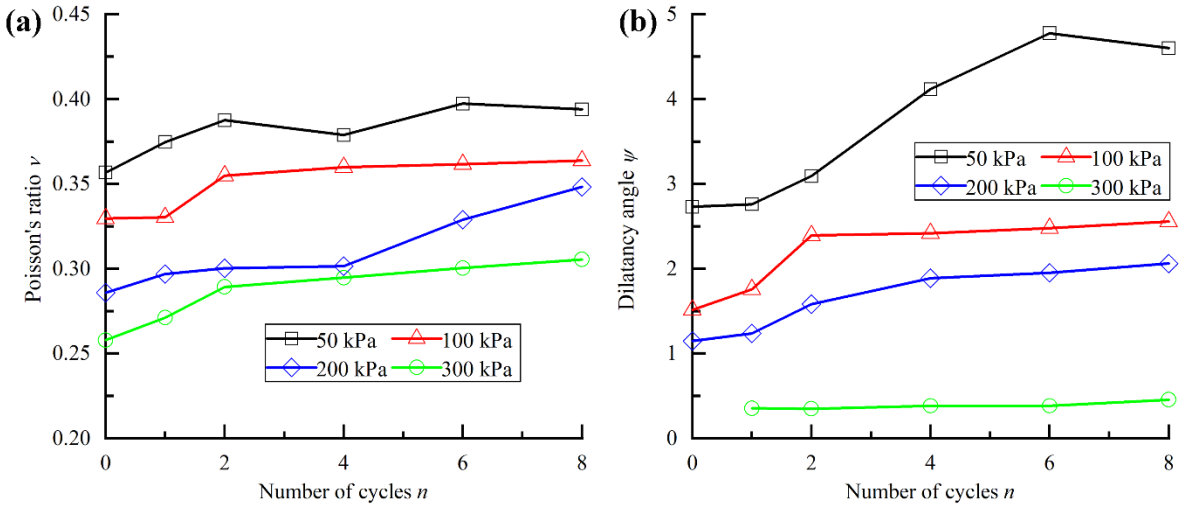

Fig. 14 Variations of Poisson's ratio and dilatancy angle with the number of WDFT cycles: (a) Poisson's ratio, and (b) dilatancy angle

3.5 Microstructure analysis and deterioration mechanism of swelling mudstone

Fig. 15 depicts the cumulative mercury intrusion and density function curves of the as-compacted specimen and those subjected to various WDFT cycles. From the cumulative curves, three fast rises for the as-compacted specimen but two fast rises for the specimens subjected to WDFT cycles could be observed (Fig. 15a). The total intruded void ratio decreased after WDFT cycles because of slight volume shrinkage [33]. From the density function curves it was observed that the as-compacted specimen exhibited a trimodal porosity with a large pore population with a mean pore diameter of 11 μm, a medium pore population with a mean diameter of 0.55 μm and a small pore population with a mean diameter of 15 nm. According to the studies of Thom et al. [47] and Wang et al. [48], 2 μm was used to separate the intra-aggregate and inter-aggregate pores. The calculated void ratios of intra-aggregate and inter-aggregate pores for the specimens before and after various WDFT cycles are summarised in Table 2. It appeared that the WDFT cycles ~~increased~~ decreased the intra-aggregate pore volume and ~~decreased~~ increased the inter-aggregate pore volume. This increase of inter-aggregate pores could be ascribed to the combined effects of the increasing suction during

drying and the formation of ice lenses during freezing process. While the specimens were dried, the aggregates were pulled apart by the increasing matric suction, and cracks appeared once the pulling stress is larger than the tensile strength. In the subsequent freezing process, the water would freeze with an increasing volume, and push away the adjacent aggregates. This facilitated to the propagation of cracks and enlargement of large pores [49]. The visual view of the specimens before and after various WDFT cycles is presented in Fig. 16. After the first cycle, several cracks initiated on the surface of specimen. With the further WDFT cycles, more and more cracks appeared and the pre-existing cracks became wider and longer. These cracks destructed the links between the aggregates and reduced the cohesion of aggregates. Thereby, a decrease of effective cohesion was observed in Fig. 12a. Meanwhile, the increasing suction during drying could induce void collapse inside aggregates, resulting in the decrease of the intra-aggregate pores (Table 2). This collapse was irreversible during the following wetting process [30, 50]. Thus, after WDFT cycles, more compact and rigid aggregates could be expected, giving rise to a larger internal friction (Fig. 12b). Additionally, the developed contacts between compact aggregates would favourite more dilative behaviour (Fig. 14b).

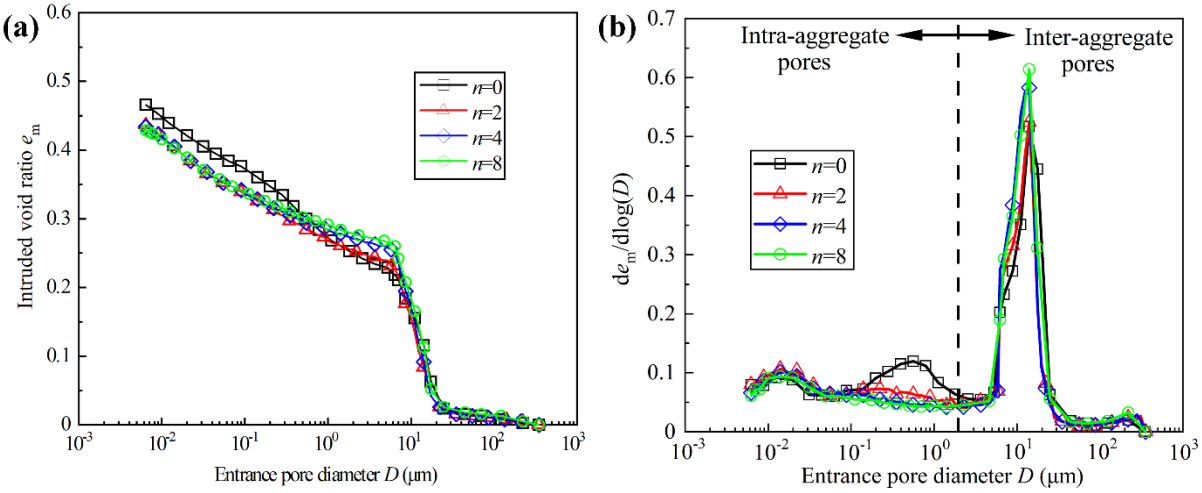

Fig. 15 MIP results of specimens before and after different WDFT cycles: (a) cumulative intruded void ratio curves, and (b) density function curves

Table 2 Intra-aggregate and inter-aggregate void ratios of the mudstone after various WDFT cycles

Cyclic number	n=0	n=2	n=4	n=8
Inter-aggregate void ratio	0.125	0.250	0.256	0.272
Intra-aggregate void ratio	0.340	0.218	0.174	0.158

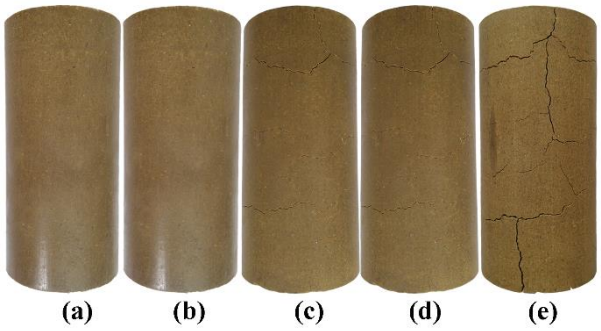

Fig. 16 The photos of specimens before and after different WDFT cycles: (a) n=0 (before WDFT cycles), (a) n=1, (c) n=2, (d) n=4, and (e) n=8

4 Modelling of mechanical behaviour subjected to WDFT cycles

In geotechnical engineering, constitutive model is very important for mechanical prediction. Stress-strain relation is a measure of material stiffness and shear strength under different circumstances and a key input parameter for mechanistic-empirical geotechnical engineering design method. As discussed above, the specimens exhibited remarkable strain-softening bahaviour after WDFT cycles in this study. Although the Modified Cam Clay (MCC) model [51] has been widely used in describing many important features of the mechanical behaviour of clay, it is limited to the softening simulation of the soils in a heavily overconsolidated state. For most clayey deposits, MCC often underestimates the softening degree. As for other MCC-based models, such as the enforced strain-softening model [52] and Structured Cam Clay (SCC) model [53], the model parameters are increasingly complex and the models are not easily realizable. In this work, to capture the strain-softening behaviour, a three-parameter nonlinear elastic constitutive model was proposed:

$$q=\frac{\varepsilon_1(a+c\varepsilon_1)}{(a+b\varepsilon_1)^2} \tag{12}$$

where a, b, and c are the parameters related to specimen property. The first-order derivative $dq/d\varepsilon_1$ can be derived as follows:

$$\frac{dq}{d\varepsilon_1}=\frac{(a+2c\varepsilon_1)(a+b\varepsilon_1)-2b\varepsilon_1(a+c\varepsilon_1)}{(a+b\varepsilon_1)^3} \tag{13}$$

The slope of the tangent line at the initial stage is the elastic modulus E_0:

$$E_0=\frac{dq}{d\varepsilon_1}\bigg|_{\varepsilon_1=0}=\frac{1}{a} \tag{14}$$

Then, the relationship between the elastic modulus and parameter a can be written as:

$$a=\frac{1}{E_0} \tag{15}$$

To find the critical point of $\varepsilon_{1\text{-max}}$, setting $dq/d\varepsilon_1$ equal to zero yields:

$$\varepsilon_{1\text{-max}}=\frac{a}{b-2c} \tag{16}$$

By substituting $\varepsilon_{1\text{-max}}$ into Eq. (12), the peak deviator stress can be derived:

$$q_p=\frac{1}{4(b-c)} \tag{17}$$

When the axial stain reaches to a very large value (tend to infinity), the deviator stress remains at a residual value (q_r). The value of residual deviator stress can be calculated using the equation below:

$$q_r=\lim_{\varepsilon_1\to\infty}\frac{\varepsilon_1(a+c\varepsilon_1)}{(a+b\varepsilon_1)^2}=\frac{c}{b^2} \tag{18}$$

By combining Eqs. (17) and (18), parameters b and c can be calculated using Eqs. (19) and (20), respectively:

$$b=\frac{1-\sqrt{1-q_r/q_p}}{2q_r} \tag{19}$$

$$c=\frac{2-q_r/q_p-2\sqrt{1-q_r/q_p}}{4q_r} \tag{20}$$

According to Eq. (15), the model parameter a represents the elastic modulus. The higher the value of a, the larger the elastic modulus. Based on Eqs. (17-18), the difference between parameters b and c reflects the peak shear strength while the ratio of c to b^2 is equal to the residual shear strength. The

higher difference between b and c and ratio of c to b^2 mean a lower peak shear strength and a larger residual shear strength, respectively. As remarked earlier, Eqs. (6-9) describe the relationships between the effective cohesion, effective friction angle and the number of WDFT cycles. Thus, the shear strength parameters at peak and critical states for the specimens after various WDFT cycles can be obtained using Eqs. (6-9). Correspondingly, the shear strengths at peak and critical states for the specimens under various confining pressures can be calculated based on the relationship between the axial stress σ_1 and confining pressure σ_3 described by the Mohr-Coulomb criterion:

$$\sigma_1=\frac{2c\cdot\cos\phi}{1\text{-}\sin\phi}+\frac{1\text{-}\sin\phi}{1\text{-}\sin\phi}\sigma_3 \tag{21}$$

where ϕ and c are the effective friction angle and effective cohesion at peak or critical state, respectively. According to the calculated peak and residual shear strengths at various confining pressures, the values of parameters a and b can be obtained for the specimens after different WDFT cycles using Eqs. (19) and (20). Based on the calculated peak shear strength, the elastic modulus can be obtained. The obtained elastic modulus is employed to calculate parameter a according to Eq. (15). The obtained values of parameters a, b, and c are also summarised in Table 3.

According to the obtained parameters, the deviator stress-axial strain relationship for specimens before and after various confining pressures can be predicted using Eq. (12). The proposed model presents an effective description of the strain-softening behaviour of the as-compacted specimens and those subjected to WDFT. The deviator stress-axial strain curves were then compared with the experimental results in Fig. 17. A satisfactory agreement was obtained between the estimated and the measured mechanical behaviour, showing the good performance of

401 the proposed model. The proposed model could well take the detrimental effect of WDFT cycles
402 into account on the mechanical behaviour of the swelling mudstones in seasonally frozen regions.

403 **Table 3** The parameter values in the proposed model

n	σ_3 (kPa)	a ($\times10^{-5}$)	b ($\times10^{-3}$)	c ($\times10^{-4}$)
0	50	3.698	1.291	3.711
	100	3.061	1.070	3.408
	200	2.277	0.807	2.918
	300	1.813	0.655	2.569
1	50	4.149	1.344	2.780
	100	3.324	1.082	2.760
	200	2.378	0.793	2.512
	300	1.851	0.635	2.274
2	50	4.478	1.414	2.358
	100	3.504	1.108	2.478
	200	2.441	0.788	2.298
	300	1.873	0.620	2.071
4	50	4.840	1.518	2.103
	100	3.691	1.151	2.331
	200	2.503	0.791	2.161
	300	1.893	0.610	1.917
6	50	4.979	1.567	2.076
	100	3.760	1.171	2.317
	200	2.524	0.793	2.123
	300	1.899	0.606	1.862
8	50	5.028	1.589	2.105
	100	3.783	1.182	2.349
	200	2.531	0.797	2.145
	300	1.901	0.608	1.876

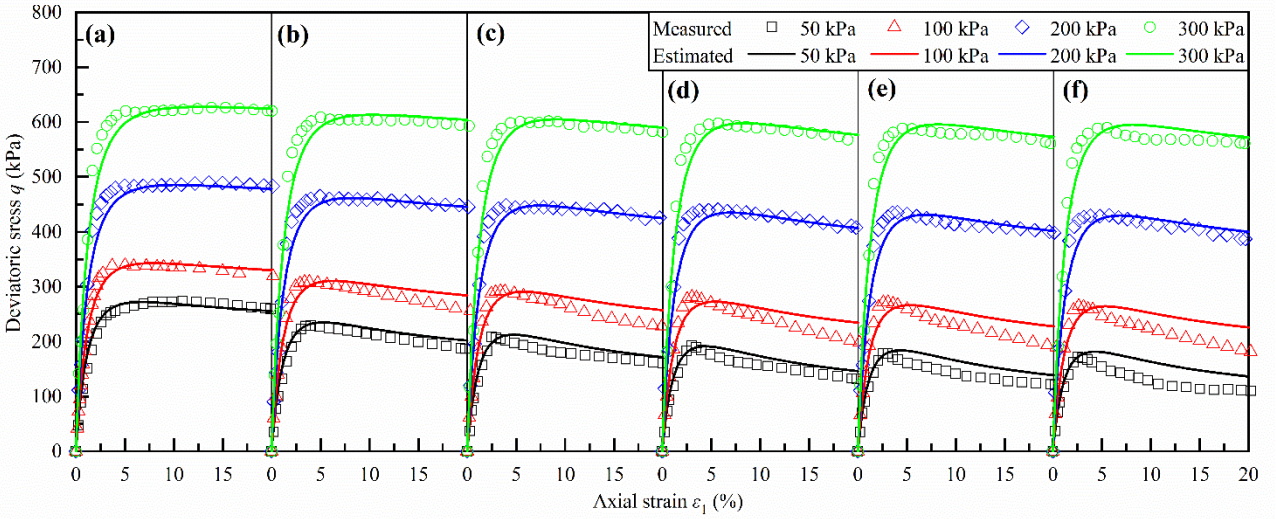

404

405 **Fig. 17** Predicted stress-strain curves of specimens before and after various WDFT cycles: (a) n=0
406 (before WDFT cycles), (a) n=1, (c) n=2, (d) n=4, (e) n=6, and (f) n=8

5 Conclusions

In this study, the effect of WDFT cycles on the mechanical behaviour of Yanji mudstone and the involved mechanism were investigated by carrying out a series of CD triaxial tests and microstructure investigation. A nonlinear elastic constitutive model was then proposed to predict the mechanical behaviour the mudstone subjected to WDFT cycles. According to the obtained results, the following conclusions are drawn:

(1) From the microstructure analysis, drying and freezing processes could induce cracks on the specimen surface and destroyed the links between aggregates, resulting in an increase of the inter-aggregate pore volume. Meanwhile, the increasing suction during drying would lead to the void collapse inside aggregates and the contraction of aggregates. As a result, the aggregates became more rigid and compact with a decrease of the intra-aggregate pore volume after WDFT cycles.

(2) From CD triaxial tests, it was observed that the specimens exhibited more significant strain-softening and dilative behaviour after WDFT cycles. The elastic modulus, and peak and residual shear strengths decreased with the increase of WDFT cycles and the decreasing rate tended to stabilization after four cycles. The lower the confining pressure, the more significant the influence of WDFT cycles. As the number of WDFT cycles increased, the effective cohesion at both the peak and critical states decreased due to the deconstruction of aggregates while the effective friction angle at both the peak and critical states increased slightly owing to the more compact aggregates. Moreover, the Poisson's ratio and dilatancy angle increased because of the more rigid contacts between aggregates after WDFT cycles.

(3) According to strain-softening behaviour, a nonlinear elastic constitutive model considering the detrimental effect of WDFT cycles was proposed to predict the mechanical behaviour of swelling mudstone in seasonally frozen regions. A satisfactory agreement between the predicted and measured stress-strain behaviour was identified, indicating the good prediction performance of the proposed method.

CRediT authorship contribution statement

Zhixiong Zeng: Conceptualization, Investigation, Formal analysis, Writing - original draft; Ling-Wei Kong: Methodology, Writing - review & editing; Yu-Jun Cui: Methodology, Writing- review & editing

Declaration of Competing Interest

The authors declare that they have no known competing financial interests or personal relationships that could have appeared to influence the work reported in this paper.

Acknowledgments

The work presented in this paper was supported by the National Key Research and Development Program of China (Grant No. 2019YFC1509901).

Data availability

Data will be made available on request.

References

1. Alonso EE, Gens A, Hight DW (1987) Special problems soils General Rep. In: European Conference on Soil Mechanics and Foundation Engineering, Dublin, Ireland

2. Chen XO, Lu ZW, He XF (1985) Moisture movement and deformation of expansive soils. In Proceeding of 14th International Conference on Soil Mechanics and Foundation Engineering, San Francisco, California, 2389-2392

3. Chen FH (1975) Foundations on expansive soils. Elsevier Science, Amsterdam

4. Massat L, Cuisinier O, Bihannic I, Claret F, Pelletier M, Masrouri F, Gaboreau S (2016) Swelling pressure development and interaggregate porosity evolution upon hydration of a compacted swelling clay. Appl Clay Sci 124–125:197–210

5. Tripathy S, Subba Rao KS, Fredlund DG (2002) Water content–void ratio swell-shrink paths of compacted expansive clays. Can Geotech J 39(4): 938–959

6. Zhao GT, Han Z, Zou WL, Wang XQ (2021) Evolution of mechanical behaviours of an expansive soil during drying-wetting, freeze–thaw, and drying-wetting-freeze–thaw cycles. Bulletin of Engineering Geology and the Environment 80(10): 8109-8121

7. Zou WL, Han Z, Zhao GT, Fan KW, Vanapalli SK, Wang XQ (2022) Effects of cyclic freezing and thawing on the shear behaviors of an expansive soil under a wide range of stress levels. Environmental Earth Sciences 81(3): 1-14

8. Jones LD, Jefferson I (2012) Expansive soils, In: BURLAND J (ed.) ICE manual of geotechnical engineering: geotechnical engineering principles, problematic soils and site investigation. Vol 1. ICE Publishing, London, UK 413-441

9. Shi B, Jiang H, Liu, Z., Fang HY (2002) Engineering geological characteristics of expansive soils in China. Eng Geol 67(1): 63–71

10. Turkoz M, Tosun H (2011) A GIS model for preliminary hazard assessment of swelling clays, a case study in Harran plain (SE Turkey). Environmental Earth Sciences 63(6): 1343-1353

11. Turkoz M, Savas H, Acaz A (2014) The effect of magnesium chloride solution on the engineering properties of clay soil with expansive and dispersive characteristics. Applied Clay Science 101: 1-9

12. Zhang YS, Qu YX, Liu GL, Wu SR (2003) Engineering geological properties of Miocene hard clays along the middle line of the North–South Diversion Water Project in China. Bull Eng Geol Environ 62(3): 213–219
13. Bensallam S, Bahi L, Alaoui M, Ejjaaouani H, Shakhirev V (2014) The effect of overpressure on the vertical cyclic deformations for clayey expansive soils in Morocco. Geosci J 18 (1): 81-87
14. Estabragh AR, Parsaei B, Javadi AA (2015) Laboratory investigation of the effect of cyclic wetting and drying on the behaviour of an expansive soil. Soils Found 55(2): 304-314
15. Villar MV, Lloret A (2008) Influence of dry density and water content on the swelling of a compacted bentonite. Appl Clay Sci 39(1-2): 38-49
16. Cui SL, Zhang HY, Zhang M (2012) Swelling characteristics of compacted GMZ bentonite–sand mixtures as a buffer/backfill material in China. Eng Geol 141: 65-73
17. Komine H, Ogata N (1994) Experimental study on swelling characteristics of compacted bentonite. Can Geotech J 31(4): 478-490
18. Zeng ZX, Cui YJ, Talandier J (2021) Compaction and sealing properties of bentonite/claystone mixture: Impacts of bentonite fraction, water content and dry density. Engineering Geology 287: 106122
19. Kong LW, Zeng ZX, Bai W, Wang M (2018) Engineering geological properties of weathered swelling mudstones and their effects on the landslides occurrence in the Yanji section of the Jilin-Hunchun high-speed railway. Bull Eng Geol Environ 77: 1491–1503
20. Sharma K, Okuno D, Munekata W (2012) Slaking effect on shear deformation and creep deformation of mudstone. Proc. 13th international summer symposium, Kyoto Japan 39-42
21. Sharma K, Kiyota T, Kyokawa H (2013) Effect of slaking on the engineering behaviour of the crushed mudstones. Bulletin of Earthquake Resistant Structure Research Center (ERS) 46: 73–82
22. Adem H, Vanapalli S (2016) Soil–environment interactions modeling for expansive soils. Environmental Geotechnics 3(3): 178–187

504 23. Chen R, Ng CWW (2013) Impact of wetting-drying cycles on hydro- mechanical behavior of an
505 unsaturated compacted clay. Applied Clay Science 86: 38-46
506 24. Erguler ZA, Shakoor A (2009) Relative contribution of various climatic processes in
507 disintegration of clay-bearing rocks. Eng Geol 108(1–2): 36–42
508 25. Li K, Nowamooz H, Chazallon C, Migault B (2018) Zarka shakedown modelling of expansive
509 soils subjected to wetting and drying cycles. Geomechanics and Geoengineering 13(2): 77-87
510 26. Subba Rao KS, Tripathy S (2009) Cyclic Swell–Shrink Behaviour of a Compacted Expansive
511 Soil. Geotechnical and Geological Engineering 27(1): 89-103
512 27. Nowamooz H, Masrouri F (2010) Influence of suction cycles on the soil fabric of compacted
513 swelling soil. Compted Rendus Geoscience 342: 901–910
514 28. Nowamooz H, Masrouri F (2010) Mechanical behaviour of expansive soils after several drying
515 and wetting cycles. Geomechanics and Geoengineering 5(4): 213–221
516 29. Tang C, Shi B, Liu C, Zhao L, Wang B (2008) Influencing factors of geometrical structure of
517 surface shrinkage cracks in clayey soils. Eng Geol 101(3): 204–217
518 30. Alonso EE, Romero E, Hoffmann C, Garc á-Escudero E (2005) Expansive bentonite–sand
519 mixtures in cyclic controlled-suction drying and wetting. Eng Geol 81(3): 213-226
520 31. Han Y, Wang Q, Wang N, Wang J, Zhang X, Cheng S, Kong Y (2018) Effect of freeze-thaw
521 cycles on shear strength of saline soil. Cold Regions Science and Technology 154: 42-53
522 32. Lu Y, Liu S, Weng L, Wang L, Li Z, Xu L (2016) Fractal analysis of cracking in a clayey soil
523 under freeze–thaw cycles. Engineering Geology 208: 93-99
524 33. Zeng ZX, Kong LW, Wang M, Sayem HM (2018) Assessment of engineering behaviour of an
525 intensely weathered swelling mudstone under full range of seasonal variation and the
526 relationships among measured parameters. Can Geotech J 55(12): 1837–1849
527 34. Nguyen TTH, Cui YJ, Ferber V, Herrier G, Ozturk T, Plier F, Tang AM (2019) Effect of
528 freeze-thaw cycles on mechanical strength of lime-treated fine-grained soils. Transportation
529 Geotechnics 21: 100281
530 35. Tang AM, Hughes PN, Dijkstra TA, Askarinejad A, Brencic M, Cui YJ, Diez JJ, Firgi T,
531 Gajewska B, Gentile F, Grossi G, Jommi C, Kehagia F, Koda E, ter Maat HW, Lenart S,

Lourenco S, Oliveira M, Osinski P, Springman SM, Stirling R, Toll DG, Van Beek V (2018) Atmosphere-vegetation-soil interactions in a climate change context; impact of changing conditions on engineered transport infrastructure slopes in Europe. Quarterly Journal of Engineering Geology and Hydrogeology

36. Hotineanu A, Bouasker M, Aldaood A, Al-Mukhtar M (2015) Effect of freeze–thaw cycling on the mechanical properties of lime-stabilized expansive clays. Cold Reg Sci Technol 119: 151-157

37. Benson CH, Othman MA (1993) Hydraulic conductivity of compacted clay frozen and thawed in situ. ASCE Journal of Geotechnical Engineering 119(2): 276– 294

38. Chamberlain EJ, Gow AJ (1979) Effect of freezing and thawing on the permeability and structure of soils. Eng Geol 13(1): 73–92

39. Zou WL, Ding LQ, Han Z, Wang XQ (2020) Effects of freeze-thaw cycles on the moisture sensitivity of a compacted clay. Engineering Geology 278: 105832

40. Zhao GT, Zou WL, Han Z, Wang DX, Wang XQ (2021) Evolution of soil-water and shrinkage characteristics of an expansive clay during freeze-thaw and drying-wetting cycles. Cold Regions Science and Technology 186: 103275

41. Zhu R, Cai Z, Huang Y, Zhang C, Guo W, Wang Y (2022) Effects of wetting-drying-freezing-thawing cycles on mechanical behaviors of expansive soil. Cold Regions Science and Technology 193: 103422

42. Ministry of Water Resources, PR China (1999) Standard for soil test method (GB/T50123–1999). China Planning Press, Beijing (in Chinese)

43. Zeng ZX, Kong LW (2019) Effect of wetting–drying–freezing–thawing cycles on the swelling behaviour of the Yanji mudstone. Environ Earth Sci 78(15): 435

44. ASTM D7181 (2020) Standard Test Method for Consolidated Drained Triaxial Compression Test for Soils

45. Lee W, Bohra NC, Altschaeffl AG (1995) Resilient modulus of cohesive soil and the effect of freeze-thaw. J Can Geotech 32: 559–568

559 46. Vermeer PA, De Borst R (1984) Non-associated plasticity for soils, concrete and rock. HERON,
560 29 (3)
561 47. Thom R, Sivakumar R, Sivakumar V, Murray EJ, Mackinnon P (2007) Pore size distribution of
562 unsaturated compacted kaolin: the initial states and final states following saturation.
563 Géotechnique 57(5): 469-474
564 48. Wang Q, Cui YJ, Tang AM, Barnichon JD, Saba S, Ye WM (2013) Hydraulic conductivity and
565 microstructure changes of compacted bentonite/sand mixture during hydration. Eng Geol 164:
566 67-76
567 49. Zeng ZX, Kong LW, Wang M, Wang J (2020) Effects of remoulding and
568 wetting-drying-freezing-thawing cycles on the pore structures of Yanji mudstones. Cold
569 Regions Science and Technology, 174: 103037
570 50. Tang CS, Cui YJ, Tang AM, Shi B (2010) Experiment evidence on the temperature dependence
571 of desiccation cracking behavior of clayey soils. Eng Geol 114(3–4): 261-266
572 51. Roscoe KH, Burland JB (1968) On the generalized stress-strain behavior of 'wet' clay,
573 Engineering Plasticity (edited by J. Heyman and F.A. Leckie), Cambridge University Press:
574 535-609
575 52. Carter JP, Liu MD (2005) Review of the structured Cam clay model, Soil Constitutive Models:
576 Evaluation, Selection and Calibration, ASCE, Geotechnical Special Publication 128: 99-132
577 53. Chai JC, Carter JP, Hayashi S (2007) Modelling strain-softening behaviour of clayey soils.
578 Lowland Technology International, 9(2): 29-37